PAPER

Check for updates

Ionic liquid exfoliated Ti₃C₂Tₓ MXene nanosheets for photoacoustic imaging and synergistic photothermal/chemotherapy of cancer†

Beibei Lu,[ab] Shunyou Hu, [ID] [ab] Dong Wu,[ab] Chengyu Wu,[ab] Zhenye Zhu, [ID] [ab] Lu Hu*[c] and Jiaheng Zhang [ID] *[ab]

$Ti_3C_2T_x$ MXene is a new type of two-dimensional material with good biocompatibility and a good photothermal effect, and shows great potential in cancer treatment. In this study, few-layer ionic liquid (IL)-$Ti_3C_2T_x$ MXene nanosheets were synthesized using IL stripping technology, which have high chemical stability, and allow photoacoustic imaging and synergistic photothermal/chemotherapy of cancer. Under 808 nm laser irradiation, the nanosheets have strong absorption in the near-infrared region, and high photothermal conversion efficiency (∼63.91%). Using DOX as a model drug, the IL-$Ti_3C_2T_x$ MXene@DOX nanosheets exhibited high drug loading capacity and pH-/photosensitivity, which will further promote the drug release of the nanosheets in an acidic tumor microenvironment and under 808 nm laser irradiation. *In vitro* and *in vivo* experiments showed that IL-$Ti_3C_2T_x$ MXene@DOX has good biological safety, allows remarkable photoacoustic imaging, and can effectively kill cancer cells with synergistic photothermal/chemotherapy. Therefore, IL-$Ti_3C_2T_x$ MXene nanosheets are expected to provide powerful and useful two-dimensional nanoplatforms for various biomedical applications.

1. Introduction

In 2011, Naguib and Barsoum *et al.*[1] discovered that hydrofluoric acid (HF) can selectively etch the three-dimensional layered compound Ti_3AlC_2. After removing the Al atomic layer by etching, the layered compound Ti_3C_2 obtained a two-dimensional (2D) graphene-like structure.[2] MXenes are composed of a MAX phase, which consists of different layered 2D transition metal carbides, nitrides, and carbonitrides. MXenes are represented by the general formula $M_{n+1}X_nT_x$, where M is a transition metal; A represents an element of group IIIA or IVA; X is C and/or N; n is generally 1, 2, or 3; and T_x represents –OH, –O, or –F and other surface groups. The MAX phase contains covalent bonds, ionic bonds, and metal bonds, wherein the M–A atomic layers are mainly formed using metal bonds. Since the bonding force between the M and A atomic layers is weaker than that between the M and X atomic layers, the A layer has higher activity and is easily exfoliated into

MXenes.[3–5] Different etchants will affect the size, degree of defects, and surface chemistry of the nanosheets, and then affect the performance of the nanosheets. The surface of the etched MXene material is loaded with a large number of functional groups, exhibiting excellent photothermal performance; the large specific surface area shows unique physical and chemical characteristics, which are beneficial for enhancing the chemical reactivity and hydrophilicity of the MXene material. The MXene materials not only have important applications in the fields of energy storage and sensing devices but have broad application prospects in the field of biomedicine.[6–9]

The MAX phase is relatively stable and has strong resistance to acid and alkali corrosion. Therefore, in the preparation of MXene materials the metal bonds can only be destroyed by chemical etching.[10] With increasing research on MXene materials, their preparation methods are constantly improved and expanded. At present, MXenes are mainly obtained by selective etching of the A atom in the precursor MAX phase using high concentration HF, a fluoride salt method, and a hydrothermal alkali etching method. However, the direct use of these methods will reduce the safety of MXene production. To avoid the use of harmful chemical substances and improve the process safety, a large number of researchers have been looking for HF-free corrosion methods to replace HF.[11]

For example, Halim *et al.*[12] used ammonium hydrogen fluoride (NH_4HF_2) instead of HF and successfully prepared

[a] *Sauvage Laboratory for Smart Materials, Harbin Institute of Technology, Shenzhen 518055, P. R. China. E-mail: zhangjiaheng@hit.edu.cn*

[b] *Research Centre of Printed Flexible Electronics, School of Materials Science and Engineering, Harbin Institute of Technology, Shenzhen 518055, P. R. China*

[c] *Guangdong Marubi Biotechnology Co., Ltd, Guangzhou 510000, P. R. China. E-mail: hu.lu@marubi.cn*

† Electronic supplementary information (ESI) available. See DOI: 10.1039/d1tb01938d

Ti_3C_2 nanosheets with larger interlayer spacing. These nanosheets are arranged in a regular structure, which improves the electron transport ability of Ti_3C_2 nanosheets. Zhang *et al.*[13] first used alkali to etch the MAX phase to prepare MXene nanosheets with F groups at the terminal, which weakened the electrochemical performance of the material. Shi *et al.*[14] used Ti_3AlC_2 as the research object and successfully synthesized biocompatible Ti_3C_2 nanosheets using a two-step method combining HF etching and tetrapropylammonium hydroxide intercalation. Dong *et al.*[15] synthesized ultrathin Ti_3C_2 MXene nanosheets ($\sim$100 nm) by supplying additive Al^{3+} to avoid Al loss and synergistic photothermal/photodynamic for cancer therapy. Although in these methods HF has been replaced and the safe production of MXenes is improved, some researchers still hope to further develop a natural, green, and pollution-free solvent for the etching MAX phase.

Encouragingly, Presser *et al.*[16] used an ionic liquid (IL) as an etchant to produce MXene nanosheets from the MAX phase without acid. During the stripping process, ILs can be used as both an etching agent and an intercalation agent to create a larger interlayer spacing, which can adjust the performance of MXenes. Zhu *et al.*[17] used an imidazole-based IL to protect the sensitivity of $Ti_3C_2T_x$ nanosheets from degradation, significantly improving the chemical stability of $Ti_3C_2T_x$ nanosheets in an aqueous environment and promoting the assembly of independent $Ti_3C_2T_x$ films. In addition, the crystal structure of IL-MXene nanosheets can remain for 30 days and the 2D layered structure in an aqueous solution can be maintained for eight months.[18] Imidazolium salts are well-known room-temperature ILs, which have been shown to prevent the nanosheets from being oxidized.[19–21]

Compared with organic solvents, ILs have unique characteristics such as non-volatility, good solubility, non-toxicity, safety, high thermal stability, and potential for solvent recovery.[22–24] Because of these characteristics, ILs have been proposed as a green alternative to traditional molecular solvents for the exfoliation of layered materials (graphene,[25] transition metal chalcogenides,[26] boron nitride,[27] and black phosphorus[28]). Most importantly, the surface tension of ILs closely matches the surface energy of graphite, which is a key condition for the direct exfoliation of graphite.[25,29] Therefore, ILs are expected to be suitable as green solvents for stripping and intercalation of Ti_3AlC_2. However, there are not many studies on the use of IL-assisted exfoliation of Ti_3AlC_2. The main advantages of ILs as multifunctional exfoliating solvents are the low costs, recyclability, high viscosity, and complete separation from the processing system.

In this study, imidazole-based ILs with different carbon chain lengths were used as etchants and intercalators to produce MXene nanosheets from the MAX phase without acid. IL-$Ti_3C_2T_x$ MXene nanosheets were prepared by the IL exfoliating method, in which a chemotherapeutic drug (DOX) was encapsulated in IL-$Ti_3C_2T_x$ MXene to further prepare multifunctional IL-$Ti_3C_2T_x$ MXene@DOX nanosheets. Studies found that IL-$Ti_3C_2T_x$ MXene@DOX exhibited high chemical stability and good biocompatibility. The drug release showed that IL-$Ti_3C_2T_x$ MXene@DOX can

Scheme 1 Schematic illustration of the preparation of few-layer $Ti_3C_2T_x$ MXene nanosheets with high chemical stability using an IL-assist exfoliating method. The nanosheets can be used for photoacoustic imaging and the synergistic photothermal/chemotherapy of tumors.

release the drug under 808 nm laser irradiation. *In vitro* and *in vivo* experiments showed that compared with single-agent therapy, the IL-$Ti_3C_2T_x$ MXene@DOX nanocomposite inhibited tumor growth using synergistic photothermal therapy (PTT) and chemotherapy; photoacoustic imaging (PAI) has great potential in cancer treatment (Scheme 1). Therefore, not only the few-layer MXene nanosheets provide a new nano-platform for the construction of collaborative treatment systems but also PAI provides important methods and development directions for current medical diagnosis and treatment.

2. Experimental

2.1 Preparation of IL monomers

1-Vinylimidazole (0.94 g, 10.0 mmol) and bromoethane (n = 1; 1.62 g, 15.0 mmol) were added to 30 mL of acetonitrile. The reaction mixture was stirred for 24 h under a nitrogen atmosphere at 80 °C. After cooling to 30 °C, acetonitrile was removed using rotary evaporation. The resulting viscous liquid was dissolved in acetonitrile again, washed three times, and then recrystallized three times with absolute ethanol. Finally, the products were dried at 50 °C under vacuum. The alkanes with different carbon chain lengths were named $[C_{n+1}mim]Br$ (n = 1, 3, 5, 7, 9, 11, 13, 15).

Subsequently, Br^- and BF_4^- undergo anion exchange through a metathesis reaction.[30] To obtain the BF_4 salt, the Br salt and BF_4Na were mixed in a molar ratio of 1 : 3 and the mixture was stirred at 30 °C for 48 h, filtered and evaporated to remove excess solvent. Finally, it was dried overnight in a vacuum at 50 °C and named $[C_{n+1}mim]BF_4$ salt (n = 1, 3, 5, 7, 9, 11, 13, 15).

2.2 Synthesis of IL-$Ti_3C_2T_x$ MXene

The Ti_3AlC_2 MAX phase (180 mg) was mixed with the IL ($[C_{n+1}mim]BF_4$, 10 mL), which was flushed with argon and stirred at 80 °C for 24 h. After cooling to 30 °C, the mixture

This journal is © The Royal Society of Chemistry 2022

J. Mater. Chem. B, 2022, **10**, 1226–1235 | **1227**

was centrifuged (8000 rpm, 5 min) and washed with Milli-Q water until the pH was neutral. The powders were vacuum dried at 80 °C for 48 h and stored in a small bottle filled with argon. The final products were named IL-Ti$_3$C$_2$T$_x$ MXene.

2.3 DOX loading and release

To load DOX onto IL-Ti$_3$C$_2$T$_x$ MXene nanosheets, 2 mL DOX (2 mg mL^{-1} in DMSO) was added dropwise into the 2 mL IL-Ti$_3$C$_2$T$_x$ MXene nanosheets (2 mg mL^{-1}) in phosphate-buffered saline (PBS, 20 mM, pH 7.4). After stirring for 24 h in the dark at 30 °C, excess DOX was removed using centrifugation. IL-Ti$_3$C$_2$T$_x$ MXene@DOX was redispersed in 1 mL of deionized water and stored at 4 °C. The loading capacity (LC, w/w%) of DOX is calculated using the following equation:

$$LC = \frac{\text{Weight of loaded DOX}}{\text{Total weight of nanocomposites}} \times 100\% \qquad (1)$$

To study the drug release kinetics, 0.1 mg mL^{-1} IL-Ti$_3$C$_2$T$_x$ MXene@DOX in PBS (pH 7.4 or pH 5.0) was added into the dialysis bag (M_w = 3500 Da) and eluted with different PBS solutions (40 mL). It was shaken (300 rpm) and irradiated with 808 nm laser radiation (1.0 W cm^{-2}) for 10 min. The released samples (2 mL) were collected at different time intervals and an equal volume of fresh PBS buffer was added. The concentration of DOX released was determined using UV-vis spectrophotometry (484 nm). The control group was subjected to the same conditions but without laser irradiation.

2.4 Photothermal effect of IL-Ti$_3$C$_2$T$_x$ MXene

IL-Ti$_3$C$_2$T$_x$ MXene nanosheets in PBS (pH 7.4, 10 μg mL^{-1}) were used with 808 nm laser irradiation (1.0 W cm^{-2}) to measure the photothermal effect. The influence of the laser power density on the photothermal effect was determined using 808 nm laser irradiation of the IL-Ti$_3$C$_2$T$_x$ MXene solution with different power densities; under the same conditions, temperature changes were measured with PBS as the control group. The thermal stability of the IL-Ti$_3$C$_2$T$_x$ MXene samples was determined by 808 nm laser irradiation for 10 min and five switching cycles. At the same time, the temperature changes of the IL-Ti$_3$C$_2$T$_x$ MXene nanosheets were recorded under near-infrared (NIR) laser irradiation (808 nm, 1.0 W cm^{-2}) for 10 min using a NIR thermal imaging system. The photothermal conversion efficiency (η) of IL-Ti$_3$C$_2$T$_x$ MXene was calculated using the following formula:[15,31]

$$\eta = \frac{hS(T_{max} - T_{surr}) - Q_0}{I(1 - 10^{-A})} \qquad (2)$$

where h is the heat transfer coefficient, S is the surface area, T_{max} is the maximum temperature at equilibrium, T_{surr} is the surrounding ambient temperature, Q_0 is the heat absorption of the quartz cell, I is the laser power density and A is the absorbance of the IL-Ti$_3$C$_2$T$_x$ MXene nanosheets at 808 nm.

2.5 Synergistic effect of *in vitro* PTT and chemotherapy

The 4T1 and L929 cells were cultured in DMEM containing 10% FBS, 1% penicillin, and 1% streptomycin in a 5% CO$_2$ incubator at 37 °C. The toxicity of IL, IL-Ti$_3$C$_2$T$_x$ MXene, and IL-Ti$_3$C$_2$T$_x$ MXene@DOX to 4T1 and L929 cells was measured using the CCK-8 method. 4T1 and L929 cells were incubated in 96-well plates at a density of 5×10^3 cells per well for 24 h, the cells were divided into eight groups and different treatment methods were used: I: PBS group (control group); II: IL; III: IL-Ti$_3$C$_2$T$_x$ MXene; IV: free DOX; V: NIR; VI: IL-Ti$_3$C$_2$T$_x$ MXene@DOX (chemotherapy group); VII: IL-Ti$_3$C$_2$T$_x$ MXene + NIR (PTT group); and VIII: IL-Ti$_3$C$_2$T$_x$ MXene@DOX + NIR (synergistic therapy group), after co-incubating for 12 h. The cells were washed with PBS, and fresh culture medium was added; a laser (808 nm, 1.0 W cm^{-2}) was used to irradiate the cells for 10 min with photothermal treatment. Subsequently, all cells were co-cultured for 24 h, and then 10 μL of CCK-8 solution was added. After co-incubation for 4 h, the absorbance of the solution was determined at 450 nm using a microplate reader (BioTek, Gen5, USA). Each concentration included six replicate wells. The cell viability was calculated using the following equation:

$$\text{Cell viability } (\%) = \frac{A_{test} - A_{blank}}{A_{control} - A_{blank}} \times 100\% \qquad (3)$$

where A_{test} and $A_{control}$ represent the absorbance of cell solutions in the treatment and control groups, respectively. A_{blank} is the absorbance of the solution without cells.

2.6 Cellular uptake of IL-Ti$_3$C$_2$T$_x$ MXene

The cell uptake efficiency was studied using confocal laser scanning microscopy (CLSM) and flow cytometry analysis. 4T1 cells were incubated in a 6-well plate at a density of 1×10^5 cells per well for 24 h. 10 μg mL^{-1} of IL-Ti$_3$C$_2$T$_x$ MXene and IL-Ti$_3$C$_2$T$_x$ MXene@DOX were added, co-incubated with the cells for 4 h and then washed with PBS. The NIR treatment group was irradiated with an 808 nm laser at 1.0 W cm^{-2} for 10 min and co-incubated for another 2 h, washed and fixed with 4% formaldehyde for 30 min. The nuclei were stained with DAPI and observed with a CLSM (Nikon A1R, Japan).

In addition, 4T1 cells at a concentration of 1×10^5 cells were incubated for 24 h. IL-Ti$_3$C$_2$T$_x$ MXene@DOX nanosheets (IL-Ti$_3$C$_2$T$_x$ MXene concentration of 10 μg mL^{-1}) were added and incubated for 2 h. Then, with or without laser irradiation for 10 min, they were co-incubated for another 2 h. Then they were washed with PBS and centrifuged, and the cells were collected, and Annexin V-FITC/PI was added in a dark environment for 30 min. The cell uptake behavior of IL-Ti$_3$C$_2$T$_x$ MXene was analyzed using flow cytometry (Cyto FLEX, Beckman, USA) and untreated cells were used as a blank control.

2.7 Mouse tumor model

BALB/c mice (female, 6–8 weeks old) were purchased from Hunan Tianqin Biotechnology Co., Ltd, China (license No. SCXK (Xiang) 2019-0014). All animal experiments were conducted following the guidelines established by Jiangxi Zhonghong Boyuan Biotechnology Co., Ltd. To verify the 4T1 tumor model, 2×10^6 4T1 cells in PBS (100 μL) were subcutaneously implanted into the right side of the mice. When the tumor volume reached the required volume, the *in vivo* experiment was performed.

1228 | *J. Mater. Chem. B*, 2022, **10**, 1226–1235

This journal is © The Royal Society of Chemistry 2022

2.8 *In vivo* PAI

To evaluate the *in vivo* PAI performance of the IL-Ti$_3$C$_2$T$_x$ MXene nanosheets for subcutaneous tumors, 4T1 tumor-bearing BALB/c mice were anesthetized with sodium pentobarbital (1%) and fixed in a PAI stent. After 0, 2, 4, 6, 8, and 24 h of tail intravenous injection of IL-Ti$_3$C$_2$T$_x$ MXene nanosheets (20 mg kg^{-1}), the tumor site of PAI was determined using a high-resolution small animal ultrasound system (VisualSonics, Canada). All PAI experiments used the same parameters.

2.9 *In vivo* PTT

4T1 tumor-bearing BALB/c mice were randomly divided into five groups (I: saline, II: NIR, III: IL-Ti$_3$C$_2$T$_x$ MXene, IV: IL-Ti$_3$C$_2$T$_x$ MXene + NIR, and V: IL-Ti$_3$C$_2$T$_x$ MXene@DOX + NIR). The mice in the I group were intravenously injected with saline, and the mice in the III–V groups were intravenously injected with 20 mg kg^{-1} IL-Ti$_3$C$_2$T$_x$ MXene (100 μL). After 4 h of injection, the tumor site was irradiated for 10 min using an 808 nm laser (1.0 W cm^{-2}), and the images of the body temperatures of the mice were observed and recorded *via* infrared thermal imaging every 2 min.

2.10 *In vivo* antitumor efficacy

When the tumor size reached 100 mm^3, the 4T1 tumor-bearing BALB/c mice were randomly divided into five groups of five mice each. Then, the mice were treated with different solutions (20 mg kg^{-1}) *via* tail intravenous injection on 3, 5, 7, and 9 days, respectively. After 4 h of injection, the mouse tumor site was irradiated with an 808 nm laser (1.0 W cm^{-2}) for 10 min. The tumor volume was calculated by measuring the diameter of the tumor. The calculation formula is as follows: $V = a \times b^2/2$ (*a*: the longest diameter of the tumor, *b*: the shortest diameter of the tumor). The relative tumor volume is calculated as V/V_0, where V_0 is the initial tumor volume at the beginning of treatment. In addition, the body weights of the mice were recorded. After the treatment, all mice were humanely euthanized, and the tumor tissues were collected, fixed with paraformaldehyde, and embedded in paraffin blocks. Paraffin tissue specimens were sectioned, stained with hematoxylin and eosin (H&E), and examined under a microscope. At the same time, proliferating cell nuclear antigen immunohistochemistry (Ki-67) staining and terminal deoxynucleotidyl transferase dUTP notch end labeling (TUNEL) kits were used to detect tumor tissue apoptosis.

2.11 *In vivo* biocompatibility analysis

After the treatment, the mice were sacrificed on day 17 for systemic toxicity evaluation. The main organs (heart, liver, spleen, lungs, and kidneys) were used for H&E staining. The serum was extracted from the blood of the mice and centrifuged for 10 min to detect common liver and kidney function indexes in the serum.

2.12 Statistical analysis

All results of the release profiles and cell uptake studies were expressed as mean ± S.D. The sample size (*n*) for each statistical analysis is shown in the figure legend. The significance of the differences between the experiments and control groups was analyzed by one-way analysis of variance (ANOVA) with Turkey post-test using GraphPad Prism software. Statistical significance was set as $*p < 0.05$, $**p < 0.01$ and $***p < 0.001$.

3. Results and discussion

3.1 Design, synthesis, optimization, and characterization of [C$_{n+1}$mim]BF$_4$ ILs

Vinyl imidazole and alkane chains through an ion exchange reaction were used to prepare a series of F-containing [C$_{n+1}$mim]BF$_4$ ILs with different carbon chain lengths (Fig. S1a, ESI†). The yields of the final products of [C$_{n+1}$mim]BF$_4$ ILs were more than 90%. The digital photos showed that the [C$_{n+1}$mim]BF$_4$ ILs have good fluidity (Fig. S1b and c, ESI†). Then, the structures of the ILs were further determined using NMR (Fig. S2–S7, ESI†) and FTIR spectra (Fig. S8, ESI†), which exhibited that the chemical shifts of [C$_{n+1}$mim]BF$_4$ ILs and [C$_{n+1}$mim]Br ILs have shifted. The ^{19}F-NMR spectrum (Fig. S7, ESI†) also proved that the [C$_{n+1}$mim]BF$_4$ ILs contain the F element. Therefore, these results indicated that a series of [C$_{n+1}$mim]BF$_4$ ILs containing F elements with different carbon chain lengths were successfully designed and prepared.[30] Subsequently, by studying the physical and chemical properties (Fig. S9, S10 and Tables S1, S2, ESI†), exfoliating effects (Fig. S11 and S12, ESI†), and toxicity experiment (Fig. S13, ESI†) of [C$_{n+1}$mim]BF$_4$ IL. Therefore, the results showed that [C$_8$mim]BF$_4$ IL can be used to further exfoliate the MAX phase material.

3.2 Preparation and characterization of IL-Ti$_3$C$_2$T$_x$ MXene nanosheets

As shown in Fig. 1a, few-layer IL-Ti$_3$C$_2$T$_x$ MXene nanosheets were prepared using an IL one-step method for exfoliation, intercalation, and modification of the MAX phase. The surfaces of the IL-Ti$_3$C$_2$T$_x$ MXene nanosheets were exposed to T (O, B, F, and N). The composition and structure of the MAX phase and IL-Ti$_3$C$_2$T$_x$ MXene were analyzed using XRD. The XRD pattern in Fig. 1b showed that Ti$_3$AlC$_2$ and IL-Ti$_3$C$_2$T$_x$ MXene have high purity and crystallinity. The hexagonal close-packed structure of pure phase Ti$_3$AlC$_2$ corresponds to JCPDS PDF file card no. 52-0875, and it can be seen that the (104) peak of IL-Ti$_3$C$_2$T$_x$ MXene at 39.0° completely disappeared, indicating that the MXene was successfully obtained by etching the Al of the Ti$_3$AlC$_2$ layer with IL; it was also important that the (002) diffraction peak of Ti$_3$AlC$_2$ at 9.5° shifted to a low angle of 6.8° after etching, which was attributed to the increase in the distance between the crystal planes of IL-Ti$_3$C$_2$T$_x$ MXene after ultrasonic stripping of the IL, indicating that the Al atom was successfully removed from Ti$_3$AlC$_2$, and few layer IL-Ti$_3$C$_2$T$_x$ MXene nanosheets were prepared.[15,31–33] The Raman spectra of the Ti$_3$AlC$_2$ MAX phase before and after IL exfoliation are shown in Fig. 1c, and compared with those of the unstripped MAX phase, the peak of IL-Ti$_3$C$_2$T$_x$ MXene broadens significantly at 154 cm^{-1} after exfoliating; the peaks at 170 cm^{-1}, 390 cm^{-1}, and 615 cm^{-1} (Ti–C vibration peaks) become stronger. These

This journal is © The Royal Society of Chemistry 2022

J. Mater. Chem. B, 2022, **10**, 1226–1235 | **1229**

Fig. 1 Synthesis and characterization of IL-$Ti_3C_2T_x$ MXene nanosheets. (a) Schematic illustration of the synthesis of IL-$Ti_3C_2T_x$ MXene nanosheets. (b) XRD patterns, (c) Raman spectra, and (d) AFM image of IL-$Ti_3C_2T_x$ MXene. (e) TEM images of IL-$Ti_3C_2T_x$ MXene. The inset shows a photograph of IL-$Ti_3C_2T_x$ MXene nanosheets dispersed in water. (f) SEM images and EDS spectra (g) of IL-$Ti_3C_2T_x$ MXene. (h) HRTEM image of overall and partial magnification (left) and the corresponding selected area electron diffraction (SAED) pattern of the IL-$Ti_3C_2T_x$ MXene (right). (i) HRTEM images and corresponding FFT patterns of the IL-$Ti_3C_2T_x$ MXene. The insets show diagrams of the lattice spacing. (j) SEM elemental mapping of IL-$Ti_3C_2T_x$ MXene.

results indicate that the ILs can successfully exfoliate the MAX phase.

AFM, TEM, SEM, and energy dispersive spectroscopy (EDS) were used to further confirm the formation of IL-$Ti_3C_2T_x$ MXene nanosheets, and these results are shown in Fig. 1d–g. From the AFM height profile (Fig. 1d), IL-$Ti_3C_2T_x$ MXene nanosheets are found to have a few layers prepared by IL exfoliation. TEM and AFM images show that the average lateral size of the IL-$Ti_3C_2T_x$ MXene nanosheets is less than 200 nm (Fig. 1d and e). When the incident light was scattered by the colloidal nanosheets, the IL-$Ti_3C_2T_x$ MXene nanosheets exhibited good water dispersibility (Tyndall effect, inset in Fig. 1e).[14] As shown in Fig. S14 (ESI†), Ti_3AlC_2 has a compact and dense structure without visible delamination before etching. After etching for 24 h, Ti_3AlC_2 transformed into IL-$Ti_3C_2T_x$ MXene with a loosely stacked structure and a certain gap between the layers (Fig. 1f). From the EDS spectrum (Fig. 1g), it can be seen that there was no Al content in Ti_3AlC_2 after etching, and N, F, and B elements were detected in the IL-$Ti_3C_2T_x$ MXene.

The full and partial high-resolution TEM (HRTEM) images on the left side of Fig. 1h showed the single crystallinity of the IL-$Ti_3C_2T_x$ MXene flakes. It can be seen from the selected area electron diffraction (SAED) image of Fig. 1h on the right that the IL-$Ti_3C_2T_x$ MXene prepared in this study has hexagonal symmetry and good crystallinity; the crystal structure of IL-$Ti_3C_2T_x$ MXene was further determined by HRTEM, Fig. 1i shows the lattice fringes with an inner plane spacing of

0.266 nm, which corresponds to the (0110) facet of IL-$Ti_3C_2T_x$ MXene. The fast Fourier transform (FFT) model revealed the hexagonal structure of the base plane.[34,35] Fig. 1j shows that the element mapping of the sample confirms that the IL can not only be exfoliated but also can be modified and protected on the surface of IL-$Ti_3C_2T_x$ MXene.

3.3 Stability of IL-$Ti_3C_2T_x$ MXene nanosheets

As shown in Fig. 2a, the morphology of IL-$Ti_3C_2T_x$ MXene has still retained nano-flakes after storage for one month, indicating that the IL can increase the stability of MXene nanosheets. It can be seen from Fig. 2b that after one month of storage, the structure of IL-$Ti_3C_2T_x$ MXene nanosheets does not change significantly and there is no peak corresponding to TiO_2 in the IL-exfoliated MXene, which indicates that IL can prevent oxidation and retain the crystal structure of MXene nanosheets. At the same time, the Raman spectra (Fig. 2c) showed that the IL-$Ti_3C_2T_x$ MXene nanosheets did not have significant differences, however, the disappearance of the peak at 2800 cm^{-1} may be due to the IL having completely formed a protective film on the surface of the MXene nanosheets to prevent the MXene from being oxidized.[36–38] These results revealed that the effect of IL exfoliation and modification on the chemical structure of the $Ti_3C_2T_x$ nanosheets is negligible.

Next, we used TGA, FTIR, and XPS to analyze the functional groups on the surface of IL-$Ti_3C_2T_x$ MXene. The TGA images (Fig. S15a, ESI†) showed a significant weight loss after IL

Fig. 2 Stability of IL-$Ti_3C_2T_x$ MXene nanosheets. (a) TEM images of IL-$Ti_3C_2T_x$ MXene after 30 days of storage. The inset shows a corresponding FFT pattern. (b) XRD patterns and (c) Raman spectra of the IL-$Ti_3C_2T_x$ MXene before and after one month of storage. XPS spectra and fitting analysis of IL-$Ti_3C_2T_x$ MXene nanosheets for (d) total survey, (e) C1s, (f) Ti 2p, (g) N 1s, and (h) F1s, respectively. (i) The histogram of the integral area graph from the XPS peak fitting results of the Ti 2p and C 1s regions of IL-$Ti_3C_2T_x$ MXene. (j–m) XPS spectra of IL-$Ti_3C_2T_x$ MXene after one month of storage.

1230 | J. Mater. Chem. B, 2022, **10**, 1226–1235

This journal is © The Royal Society of Chemistry 2022

exfoliation for 24 h. The IL-Ti$_3$C$_2$T$_x$ MXene was reduced by approximately 13.58 wt%, which was higher than the weight loss of the unstripped MAX phase (11.01%). As shown in Fig. S15b (ESI†), the FTIR spectra exhibited that, compared with the MAX phase, the IL-Ti$_3$C$_2$T$_x$ MXene nanosheets have a wider absorption band, and the stretching peak was shifted. The peaks at 1637 cm^{-1} and 3409 cm^{-1} correspond to C=O and –OH groups, respectively.[39]

The change of time with the surface chemical composition of IL-Ti$_3$C$_2$T$_x$ MXene nanosheets was studied. Fig. 2d shows the full XPS spectra of IL-Ti$_3$C$_2$T$_x$ MXene –, and the peaks of Ti, C, O, N, and F can be observed in all samples; IL-Ti$_3$C$_2$T$_x$ MXene has a new peak at 400 eV belonging to N1s, which comes from ILs, indicating that IL successfully attached to the surface of the nanosheet. It can be seen from Fig. 2e that the four peaks are located at 281.4 eV, 284.9 eV, 286.8 eV, and 290.3 eV, representing C–Ti, C–C, C–H, and C–F respectively. Fig. 2f shows the Ti 2p nuclear energy spectra and fit of the data with lines; the peaks at 455.2 eV, 456.9 eV, 459.1 eV, 462.6 eV, and 464.8 eV represent Ti–C, Ti–N, Ti–O, and Ti–F, respectively. On the N 1s nuclear energy level spectra (Fig. 2g), curve fitting was performed at 401.2 eV, representing C–N; Fig. 2h shows the energy spectra of the F 1s nuclear level, in which curve fittings were performed at 684.0 eV (C–Ti–F).[8,9,40]

To detect the oxidation state of the MXene nanosheets, Fig. 2d and j–m show the XPS spectra of IL-Ti$_3$C$_2$T$_x$ MXene after one month of storage. It can be observed that the peak intensity of Ti 2p shows almost no change, indicating that there is only slight oxidation. Further analysis of the chemical composition and the atomic number of IL-Ti$_3$C$_2$T$_x$ MXene is shown in Fig. 2i, and it can be seen from the integrated area that the peaks of C and Ti show almost no obvious changes, indicating that the addition of ILs inhibited the oxidation process of Ti$_3$C$_2$T$_x$ MXene nanosheets. Therefore, these results confirmed that the IL-Ti$_3$C$_2$T$_x$ MXene nanosheets still maintained a well-layered structure after one month of storage, which also proves that ILs can prevent MXene nanosheets from being oxidized and form a protective film on the surface.[18]

3.4 Photothermal performance of IL-Ti$_3$C$_2$T$_x$ MXene nanosheets

The hydrodynamic diameter and zeta potential of IL-Ti$_3$C$_2$T$_x$ MXene were verified using DLS. As shown in Fig. 3a and Table S3 (ESI†), the particle size of the IL-Ti$_3$C$_2$T$_x$ MXene in water was approximately 164.5 nm, while the particle size in saline and DMEM was slightly smaller (114.6 nm). The hydrodynamic diameter of IL-Ti$_3$C$_2$T$_x$ MXene@DOX (191.4 nm; Fig. S16a and Tables S3, S4, ESI†) was larger than that of IL-Ti$_3$C$_2$T$_x$ MXene (164.5 nm), which also allows these nanosheets to reach the tumor site through enhanced permeability and retention effects.[31,41,42] In addition, IL-Ti$_3$C$_2$T$_x$ MXene showed good colloidal stability and could be well dispersed in water, PBS, saline, and DMEM, and the dispersions exhibit no significant change even after storage for one month (Fig. 3b). As expected, the zeta potential of IL-Ti$_3$C$_2$T$_x$ MXene in four different solutions ranges from −5.8 to −8.0 mV (Fig. 3c). The zeta

Fig. 3 Photothermal performance of IL-Ti$_3$C$_2$T$_x$ MXene nanosheets. (a) Dynamic light scattering (DLS) profile. The inset shows a photo of IL-Ti$_3$C$_2$T$_x$ MXene nanosheets in different solutions. (b) Stability of IL-Ti$_3$C$_2$T$_x$ MXene in different solutions (n = 3). (c) Zeta potential of IL-Ti$_3$C$_2$T$_x$ MXene@DOX in different solutions (n = 3). (d) UV-vis-NIR absorption spectra of IL, IL-Ti$_3$C$_2$Tx MXene, and IL-Ti$_3$C$_2$T$_x$ MXene@DOX (IL-Ti$_3$C$_2$T$_x$ MXene concentration is 10 μg mL^{-1}). (e) Photothermal profile of IL-Ti$_3$C$_2$T$_x$ MXene nanosheets in water (100 μg mL^{-1}) at a different laser power density. (f) Photothermal profile of IL-Ti$_3$C$_2$T$_x$ MXene nanosheets in water at varying concentrations (808 nm, 1.0 W cm^{-2}). (g) Photostability test of IL-Ti$_3$C$_2$T$_x$ MXene nanosheets in water under 808 nm irradiation (1.0 W cm^{-2}). (h) Photothermal heating and cooling curves of IL-Ti$_3$C$_2$T$_x$ MXene nanosheets in water. (i) Photothermal performance of free DOX, IL-Ti$_3$C$_2$T$_x$ MXene, and IL-Ti$_3$C$_2$T$_x$ MXene@DOX solutions (808 nm, 1.0 W cm^{-2}).

potential of IL-Ti$_3$C$_2$T$_x$ MXene@DOX increased to +1.29 mV (Fig. S16b and Table S4, ESI†), which further confirmed the successful addition of DOX to IL-Ti$_3$C$_2$T$_x$ MXene nanosheets. It can be seen from the fluorescence spectra (Fig. S16c, ESI†) that an obvious absorption peak of IL-Ti$_3$C$_2$T$_x$ MXene@DOX (620 nm) is present, and the UV-vis-NIR spectra show that the absorption peak of DOX is slightly red-shifted from 487 nm to 505 nm (Fig. 3d). Fig. S16d (ESI†) shows that with the increase of concentration, the absorption of IL-Ti$_3$C$_2$T$_x$ MXene also increased at 808 nm, while IL was almost absent in this region, indicating that IL-Ti$_3$C$_2$T$_x$ MXene and IL-Ti$_3$C$_2$T$_x$ MXene@DOX were successfully prepared and exhibited good absorbance in the NIR region.[39] Therefore, we chose 808 nm laser irradiation for the subsequent photothermal studies.

IL-Ti$_3$C$_2$T$_x$ MXene nanosheets can convert NIR irradiation energy into heat energy, so the photothermal conversion efficiency of IL-Ti$_3$C$_2$T$_x$ MXene aqueous dispersion solution under 808 nm laser irradiation was studied. As shown in Fig. 3e, with the increase of laser power density, the temperature of the IL-Ti$_3$C$_2$T$_x$ MXene aqueous dispersion solution also increased significantly; when the laser density was 1.0 W cm^{-2}, the temperature of the IL-Ti$_3$C$_2$T$_x$ MXene nanosheets increased to 60.84 °C. As shown in Fig. 3f, as the concentration of IL-Ti$_3$C$_2$T$_x$ MXene increased, the aqueous dispersion solution temperature also increased significantly (1.0 W cm^{-2}) relative to the temperature change of pure water. After 30 min of irradiation, no

significant changes in the IL-$Ti_3C_2T_x$ MXene nanosheets were observed. Therefore, the IL-$Ti_3C_2T_x$ MXene nanosheets exhibited good photothermal cycling stability (Fig. 3g and h). As shown in Fig. S17 (ESI†), according to the linear regression curve, the calculated photothermal conversion efficiency of the IL-$Ti_3C_2T_x$ MXene nanosheets was 63.91%, which was much higher than that reported for IL-$Ti_3C_2T_x$ nanosheets without Al^{3+} etching (30.6%).[14] In addition, the photothermal effect of the IL-$Ti_3C_2T_x$ MXene did not change significantly after DOX was loaded (Fig. 3i), which also illustrated the stability of IL-$Ti_3C_2T_x$ MXene. Owing to their excellent photothermal performance and stability, IL-$Ti_3C_2T_x$ MXene nanosheets are expected to become excellent tumor photothermal therapeutic agents.[15,43]

3.5 *In vitro* cellular uptake of IL-$Ti_3C_2T_x$ MXene nanosheets

Drug loading capacity is an important condition for IL-$Ti_3C_2T_x$ MXene nanosheets as a drug delivery system.[44,45] Fig. S18 (ESI†) shows that the loading capacity of DOX increased almost linearly with increasing concentration. When the concentration of DOX was 1 mg mL^{-1}, the drug loading was as high as $\sim$95%, which was significantly higher than those of many traditional nanosheet-based nanodrug delivery systems.[46,47] This further confirmed that the IL-$Ti_3C_2T_x$ MXene nanosheets have great potential for drug delivery. Moreover, an acidic tumor microenvironment and photothermal stimulation were used to achieve tumor specific treatment. As shown in Fig. 4a, it is interesting that the IL-$Ti_3C_2T_x$ MXene@DOX release rate was more than 10% after 10 min of 808 nm laser irradiation, which was significantly higher than that without radiation. This may be attributed to laser irradiation-generated heat (approximately 50 °C) promoting the release of DOX and the electrostatic interaction system in IL-$Ti_3C_2T_x$ MXene@DOX was destroyed. The release rate of DOX was faster at pH 5.0 than at pH 7.4, and the cumulative release was the highest at pH 5.0. The acidic microenvironment of tumor tissues and the hydrogen ions in the IL on the surface of $Ti_3C_2T_x$ MXene promoted the release of drugs in the acidic environment.[48–50] Therefore, these results indicate that pH-dependent and NIR-stimulated DOX release can effectively enhance the synergistic chemo/photothermal therapeutic effect of tumors.

In addition, without NIR laser irradiation, the cytotoxicity of DOX and IL-$Ti_3C_2T_x$ MXene@DOX was different (for the same dose of DOX, with a concentration of 10 μg mL^{-1}), maybe because ILs have certain antitumor properties. After 808 nm laser irradiation (1.0 W cm^{-2}), tumor cells have an obvious synergistic killing effect, but normal cells have no killing effect *in vitro* (Fig. 4b and Fig. S19, ESI†), because the photothermal effect of NIR laser irradiation can promote the release of DOX and killing tumor cells. Fig. S20 and Table S5 (ESI†) summarize the 50% inhibiting concentration of different IL-$Ti_3C_2T_x$ MXene nanosheets. Flow cytometry revealed that IL-$Ti_3C_2T_x$ MXene@DOX nanosheets can inhibit the growth of 4T1 tumor cells. As shown in Fig. 4c, interestingly, compared with the control group, IL-$Ti_3C_2T_x$ MXene@DOX significantly increased cell apoptosis (13.12 folds); under 808 nm laser irradiation, IL-$Ti_3C_2T_x$ MXene@DOX more effectively induced cell apoptosis (44.06-fold). Therefore, the fluorescence of tumor cells was
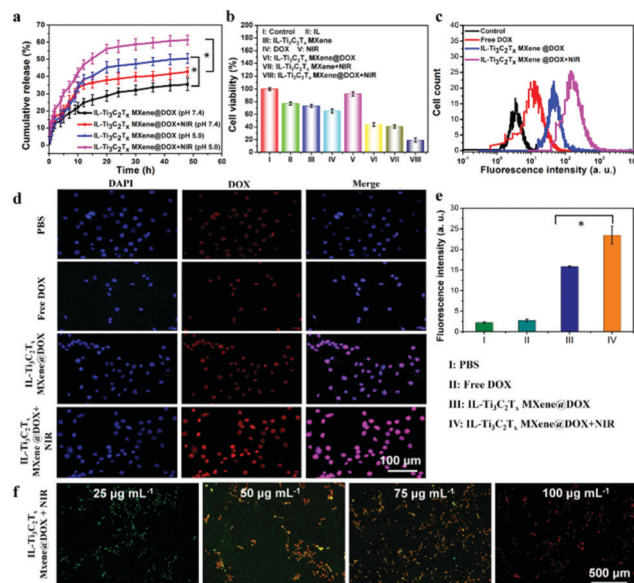

Fig. 4 *In vitro* cellular uptake of IL-$Ti_3C_2T_x$ MXene nanosheets. (a) Drug release profiles of IL-$Ti_3C_2T_x$ MXene@DOX with or without NIR laser irradiation (808 nm, 1.0 W cm^{-2}) at pH 7.4 and 5.0 ($n = 3$, *$p < 0.05$). (b) Cell viability of 4T1 cells (IL-$Ti_3C_2T_x$ MXene and DOX concentration are 10 μg mL^{-1}, respectively) ($n = 6$). (c) Flow cytometry study of 4T1 cells treated with control, free DOX, and IL-$Ti_3C_2T_x$ MXene@DOX with or without NIR laser irradiation (808 nm, 1.0 W cm^{-2}, 10 min). (d) Fluorescence images of IL-$Ti_3C_2T_x$ MXene@DOX treated 4T1 cells (scale bars: 100 μm). (e) Fluorescence intensity quantitative data of IL-$Ti_3C_2T_x$ MXene@DOX with or without NIR laser irradiation incubated with 4T1 cells ($n = 3$, *$p < 0.05$). (f) Fluorescence images of 4T1 cells stained with Calcein-AM (live cells, green fluorescence) and PI (dead cells, red fluorescence) (scale bars: 500 μm).

enhanced (Fig. 4c). Fig. 4d shows that after IL-$Ti_3C_2T_x$ MXene@DOX was co-incubated with cells for 6 h, the fluorescence of IL-$Ti_3C_2T_x$ MXene@DOX was significantly enhanced; after 10 min of NIR laser irradiation, the fluorescence of IL-$Ti_3C_2T_x$ MXene@DOX + NIR was higher than that of IL-$Ti_3C_2T_x$ MXene@DOX (1.48 fold, Fig. 4e). This may be due to the higher cell metabolism and membrane permeability of laser-induced hyperthermia, which enhances the accumulation of IL-$Ti_3C_2T_x$ MXene nanosheets in tumor cells.[43,50–52]

To further confirm the potential lethality of NIR laser irradiation on cells, calcein-Am/PI was used to mark the state of cells. When the concentration of IL-$Ti_3C_2T_x$ MXene was 100 μg mL^{-1}, IL-$Ti_3C_2T_x$ MXene effectively killed more than 95% of the 4T1 cells (Fig. 4f), which was similar to the results shown in a CLSM (Fig. 4d). Interestingly, there was a linear relationship between cancer cell apoptosis and concentration (Fig. S21, ESI†). The higher the concentration of IL-$Ti_3C_2T_x$ MXene, the more severe the cell apoptosis. Therefore, these results indicated that IL-$Ti_3C_2T_x$ MXene nanosheets have a significant inhibitory effect on tumor cells, and can effectively enhance the synergistic chemo/photothermal therapeutic effect on tumors.

3.6 *In vivo* treatment and imaging of IL-$Ti_3C_2T_x$ MXene nanosheets

The anti-tumor effect of IL-$Ti_3C_2T_x$ MXene nanosheets was determined. We established a 4T1 tumor model, and when

1232 | *J. Mater. Chem. B*, 2022, **10**, 1226–1235

This journal is © The Royal Society of Chemistry 2022

the tumor volume was up to 100 cm^3 the mice were randomly divided into five groups and 20 mg kg^{-1} of IL-Ti$_3$C$_2$T$_x$ MXene nanosheets was used as the dose for subsequent mice experiments. PTT was performed every two days, and all mice were sacrificed after 17 days. Fig. 5a summarizes the diagram of mice treatment routes. Fig. 5b records the temperature of the tumor site during PTT. The temperature of group V rapidly increased to 53.23 °C higher than that of group I (36.79 °C), after 10 min of 808 nm laser irradiation. Therefore, infrared thermal imaging further confirmed that IL-Ti$_3$C$_2$T$_x$ MXene nanosheets have good accumulation and high photothermal conversion ability at the tumor site.[51,53] Fig. 5c lists the names of each group of mice. The excellent photothermal conversion efficiency has prompted us to use IL-Ti$_3$C$_2$T$_x$ MXene nanosheets for PAI and PTT in tumors. First, the PAI ability of IL-Ti$_3$C$_2$T$_x$ MXene nanosheets at the tumor site through tail intravenous injection was observed. As shown in Fig. 5d, after injection for 2 h, a photoacoustic (PA) signal was observed in the tumor, and the PA signal at the tumor site gradually increased over time and reached the maximum at 8 h. As metabolism progresses in the body, the signal decreases 24 h after the injection. The corresponding quantitative PA average and PA average threshold are shown in Fig. 5e. Therefore, IL-Ti$_3$C$_2$T$_x$ MXene nanosheets have good PAI capabilities.[50,54]

During the treatment, the body weight and tumor volume of the mice were recorded every three days. Fig. 5f and g show that compared with the normal saline group, the tumor volume of the mice in group V was significantly reduced, but the body weight of the mice did not change, indicating that IL-Ti$_3$C$_2$T$_x$ MXene nanosheets are generally safe for *in vivo* treatment.[54] After the treatment, the antitumor effect of IL-Ti$_3$C$_2$T$_x$ MXene nanosheets was evaluated by hematoxylin and eosin (H&E), terminal deoxynucleotidyl transferase dUTP notch end labeling (TUNEL), and proliferating cell nuclear antigen immunohistochemistry (Ki-67) staining of the tumor tissue. For H&E staining (Fig. 5h), group V showed obvious tumor tissue shrinkage and damage. For TUNEL staining, I–III groups showed no green fluorescence signal, while groups IV and V showed a little green fluorescence, indicating that the tumor tissue was apoptotic in the IV and V groups and NIR irradiation has increased tumor tissue apoptosis; moreover, group V had obvious apoptosis in the tumor tissue (Ki-67 staining). Therefore, these results all indicate that IL-Ti$_3$C$_2$T$_x$ MXene can inhibit tumor growth in mice under 808 nm irradiation.[52,55]

In addition, to evaluate the side effects of IL-Ti$_3$C$_2$T$_x$ MXene on mice, we used H&E staining to study the physiological and pathological changes of the main organs (heart, liver, spleen, lungs, and kidneys) after treatment with IL-Ti$_3$C$_2$T$_x$ MXene. Compared with the normal saline group, there was no significant morphological difference in the treatment group (Fig. S22, ESI†). Fig. 5i shows that the liver function indexes (including aspartate aminotransferase and alanine aminotransferase) and renal function indexes (urea nitrogen and creatinine) are within the normal range, and there is no liver or kidney damage.[56] The results fully confirmed that IL-Ti$_3$C$_2$T$_x$ MXene nanosheets have no obvious systemic side effects and have good biological safety.
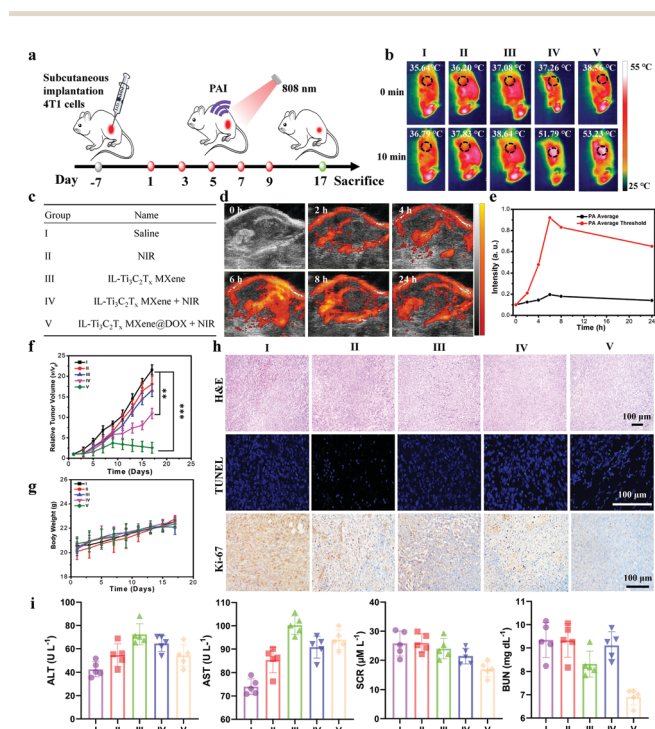

Fig. 5 *In vivo* treatment and imaging of IL-Ti$_3$C$_2$T$_x$ MXene nanosheets. (a) Schematic diagram of the drug treatment process in the subcutaneously implanted tumor model. (b) Infrared thermal imaging of tumor-bearing mice with different groups. (c) Abbreviations of different groups and names. (d) PA images of mice injected with IL-Ti$_3$C$_2$T$_x$ MXene (20 mg kg^{-1}) at different times. (e) PA average and PA average threshold of circled tumors at different time intervals. (f) Growth curves of the 4T1 tumors in mice following the indicated treatments (**$p < 0.01$ and ***$p < 0.001$). (g) Body weight changes of the tumor-bearing mice following the treatments. (h) H&E staining, TUNEL staining, and Ki-67 immunofluorescence images after the treatments in different groups (scale bar: 100 μm). (i) Hematology testing of mice in different groups (alanine aminotransferase (ALT), aspartate aminotransferase (AST), serum creatinine (SCR), and blood urea nitrogen (BUN)).

4. Conclusions

In summary, we reported a new method of IL-assisted exfoliation of the MAX phase and prepared few-layer IL-Ti$_3$C$_2$T$_x$ MXene nanosheets with an average size less than 200 nm and an average thickness of 1–4 nm. Under 808 nm laser irradiation, the IL-Ti$_3$C$_2$T$_x$ MXene nanosheets exhibited chemical stability and strong near-infrared absorption, and the photothermal conversion efficiency was as high as 63.91%. Taking DOX as a model drug, the IL-Ti$_3$C$_2$T$_x$ MXene nanosheet drug delivery system showed pH-/photosensitivity, and the drug release was accelerated in an acidic environment with 808 nm laser irradiation. *In vitro*, IL-Ti$_3$C$_2$T$_x$ MXene nanosheets exhibit good photothermal effects on 4T1 cells under 808 nm irradiation and provide a good photoacoustic image. In addition, IL-Ti$_3$C$_2$T$_x$ MXene nanosheets show good anti-tumor effects both *in vitro* and *in vivo* and have good biological safety. Therefore, IL-Ti$_3$C$_2$T$_x$ MXene nanosheets

This journal is © The Royal Society of Chemistry 2022

J. Mater. Chem. B, 2022, **10**, 1226–1235 | **1233**

could be used for photoacoustic imaging and synergistic photo-thermal/chemotherapy of cancer.

Conflicts of interest

The authors declare no conflict of interest.

Acknowledgements

Notes and references

1 M. Naguib, M. Kurtoglu, V. Presser, J. Lu, J. J. Niu, M. Heon, L. Hultman, Y. Gogotsi and M. W. Barsoum, *Adv. Mater.*, 2011, **23**, 4248–4253.

2 M. Naguib, V. N. Mochalin, M. W. Barsoum and Y. Gogotsi, *Adv. Mater.*, 2014, **26**, 992–1005.

3 H. Lin, Y. Chen and J. L. Shi, *Adv. Sci.*, 2018, **5**, 1800518.

4 W. Tao, N. Kong, X. Y. Ji, Y. P. Zhang, A. Sharma, J. Ouyang, B. W. Qi, J. Q. Wang, N. Xie, C. H. Kang, H. Zhang, O. C. Farokhzad and J. S. Kim, *Chem. Soc. Rev.*, 2019, **48**, 2891–2912.

5 B. Xu and Y. Gogotsi, *Adv. Funct. Mater.*, 2020, **30**, 2007011.

6 G. K. Nasrallah, M. Al-Asmakh, K. Rasoolc and K. A. Mahmoud, *Environ. Sci.: Nano*, 2018, **5**, 1002–1011.

7 S. H. Seok, S. Choo, J. Kwak, H. Ju, J. H. Han, W. S. Kang, J. Lee, S. Y. Kim, D. H. Lee, J. Lee, J. Wang, S. Song, W. Jo, B. M. Jung, H. G. Chae, J. S. Son and S. Y. Kwon, *Nanoscale Adv.*, 2021, **3**, 517–527.

8 B. B. Lu, Z. Y. Zhu, B. Y. Ma, W. Wang, R. S. Zhu and J. H. Zhang, *Small*, 2021, 2100946.

9 K. Y. Wang, J. S. Chen and X. B. Yan, *Nano Energy*, 2021, **79**, 105453.

10 L. Liu, G. B. Ying, D. Wen, K. C. Zhang, C. Hu, Y. T. Zheng, C. Zhang, X. Wang and C. Wang, *Mater. Des.*, 2021, **197**, 109276.

11 S. Yang, P. P. Zhang, F. X. Wang, A. G. Ricciardulli, M. R. Lohe, P. W. M. Blom and X. L. Feng, *Angew. Chem., Int. Ed.*, 2018, **57**, 15491–15495.

12 J. Halim, M. R. Lukatskay, K. M. Cook, J. Lu, C. R. Smith, L. Å. Naslund, S. J. May, L. Hultman, Y. Gogotsi, P. Eklund and M. W. Barsoum, *Chem. Mater.*, 2014, **26**, 2374–2381.

13 T. F. Li, L. L. Yao, Q. L. Liu, J. J. Gu, R. C. Luo, J. H. Li, X. D. Yan, W. Q. Wang, P. Liu, B. Chen, W. Zhang, W. Abbas, R. Naz and D. Zhang, *Angew. Chem., Int. Ed.*, 2018, **57**, 6115–6119.

14 H. Lin, X. G. Wang, L. D. Yu, Y. Chen and J. L. Shi, *Nano Lett.*, 2017, **17**, 384–391.

15 G. Y. Liu, J. H. Zou, Q. Y. Tang, X. Y. Yang, Y. W. Zhang, Q. Zhang, W. Huang, P. Chen, J. J. Shao and X. C. Dong, *ACS Appl. Mater. Interfaces*, 2017, **9**, 40077–40086.

16 S. Husmann, Ö. Budak, H. Shim, K. Liang, M. Aslan, A. Kruth, A. Quade, M. Naguib and V. Presser, *Chem. Commun.*, 2020, **56**, 11082–11085.

17 Y. J. Wan, K. Rajavel, X. M. Li, X. Y. Wang, S. Y. Liao, Z. Q. Lin, P. L. Zhu, R. Sun and C. P. Wong, *Chem. Eng. J.*, 2021, **408**, 127303.

18 X. Y. Ren, M. F. Huo, M. M. Wang, H. Lin, X. X. Zhang, J. Yin, Y. Chen and H. H. Chen, *ACS Nano*, 2019, **13**, 6438–6454.

19 C. X. Hu, Q. Xiao, Y. Y. Ren, M. Zhao, G. H. Dun, H. R. Wu, X. Y. Li, Q. Q. Yang, B. Sun, Y. Peng, F. Yan, Q. Wang and H. L. Zhang, *Adv. Funct. Mater.*, 2018, **28**, 1805311.

20 S. Walia, S. Balendhran, T. Ahmed, M. Singh, C. E. Badawi, M. D. Brennan, P. Weerathunge, M. N. Karim, F. Rahman, A. Rassell, J. Duckworth, R. Ramanathan, G. E. Collis, C. J. Lobo, M. Toth, J. C. Kotsakidis, B. Weber, M. Fuhrer, J. M. D. Vera, M. J. S. Spencer, I. Aharonovich, S. Sriram, M. Bhaskaran and V. Bansal, *Adv. Mater.*, 2017, **29**, 1700152.

21 L. Zhao, C. Y. Zhang, L. Zhuo, Y. G. Zhang and J. Y. Ying, *J. Am. Chem. Soc.*, 2008, **130**, 12586–12587.

22 P. Han, T. C. Liu, X. W. Ji and S. K. Tang, *Chin. Chem. Lett.*, 2018, **29**, 1305–1309.

23 Z. H. Xia, J. Y. Li, J. M. Zhang, X. C. Zhang, X. J. Zheng and J. Zhang, *J. Bioresour. Bioprod.*, 2020, **5**, 79–95.

24 J. M. Gomes, S. S. Silva and R. L. Reis, *Chem. Soc. Rev.*, 2019, **48**, 4317–4335.

25 X. Q. Wang, P. F. Fulvio, G. A. Baker, G. M. Veith, R. R. Unocic, S. M. Mahurin, M. F. Chi and S. Dai, *Chem. Commun.*, 2010, **46**, 4487–4489.

26 Y. Tan, M. S. Li, X. X. Ye, Z. G. Wang, Y. Y. Wang and C. Y. Li, *Sens. Actuators, B*, 2018, **262**, 982–990.

27 T. Morishita, H. Okamoto, Y. Katagiri, M. Matsushita and K. Fukumori, *Chem. Commun.*, 2015, **51**, 12068–12071.

28 W. C. Zhao, Z. M. Xue, J. F. Wang, J. Y. Jiang, X. H. Zhao and T. C. Mu, *ACS Appl. Mater. Interfaces*, 2015, **7**, 27608–27612.

29 Y. Hernandez, V. Nicolosi, M. Lotya, F. M. Blighe, Z. Y. Sun, S. De, I. T. McGovern, B. Holland, M. Byrne, Y. K. G. Ko, J. J. Boland, P. Niraj, G. Duesberg, S. Krishnamurthy, R. Goodhue, J. Hutchison, V. Scardaci, A. C. Ferrari and J. N. Coleman, *Nat. Nanotechnol.*, 2008, **3**, 563–568.

30 B. B. Lu, Y. B. Li, Z. Y. Wang, B. S. Wang, X. Pan, W. W. Zhao, X. Ma and J. H. Zhang, *New J. Chem*, 2019, **43**, 12275–12282.

31 J. R. Wu, D. H. Bremner, S. W. Niu, H. L. Wu, J. Z. Wu, H. J. Wang, H. Y. Li and L. M. Zhu, *Chem. Eng. J.*, 2018, **342**, 90–102.

32 P. Lu, J. L. Wu, X. Y. Shen, X. P. Gao, Z. F. Shi, M. Lu, W. W. Yu and Y. Zhang, *Adv. Sci.*, 2020, **7**, 2001562.

1234 | *J. Mater. Chem. B*, 2022, **10**, 1226–1235

This journal is © The Royal Society of Chemistry 2022

33 D. B. Wang, Y. X. Fang, W. Yu, L. L. Wang, H. Q. Xie and Y. Y. Yue, *Sol. Energy Mater. Sol. Cells*, 2021, **220**, 110850.

34 Q. Luo, B. Chai, M. Q. Xu and Q. Z. Cai, *Appl. Phys. A: Mater. Sci. Process.*, 2018, **124**, 495–502.

35 Q. Xue, H. J. Zhang, M. S. Zhu, Z. X. Pei, H. F. Li, Z. F. Wang, Y. Huang, Y. Huang, Q. H. Deng, J. Zhou, S. Y. Du, Q. Huang and C. Y. Zhi, *Adv. Mater.*, 2017, **29**, 1604847.

36 A. Sarycheva and Y. Gogotsi, *Chem. Mater.*, 2020, **32**, 3480–3488.

37 P. Sedlak, D. Sobola, A. Gajdos, R. Dallaev, A. Nebojsa and P. Kubersky, *Polymers*, 2021, **13**, 2678–2693.

38 W. Y. Yuan, L. F. Cheng, Y. R. An, S. L. Lv, H. Wu, X. L. Fan, Y. N. Zhang, X. H. Guo and J. W. Tang, *Adv. Sci.*, 2018, **5**, 1700870.

39 Y. Y. Ma, X. F. Lv, D. B. Xiong, X. S. Zhao and Z. H. Zhang, *Appl. Catal., B*, 2021, **284**, 119720.

40 Y. E. Shi, F. Han, L. Y. Xie, C. C. Zhang, T. Z. Li, H. G. Wang, W. F. Lai, S. J. Luo, W. Wei, Z. G. Wang and Y. Huang, *Mikrochim. Acta*, 2020, **187**, 38–46.

41 T. Liu, C. Wang, W. Cui, H. Gong, C. Liang, X. Z. Shi, Z. W. Li, B. Q. Sun and Z. Liu, *Nanoscale*, 2014, **6**, 11219–11225.

42 H. Lin, S. S. Gao, C. Dai, Y. Chen and J. L. Shi, *J. Am. Chem. Soc.*, 2017, **139**, 16235–16247.

43 Z. Liu, M. L. Zhao, H. Lin, C. Dai, C. Y. Ren, S. J. Zhang, W. J. Peng and Y. Chen, *J. Mater. Chem. B*, 2018, **6**, 3541–3548.

44 X. Y. Ji, N. Kong, J. Q. Wang, W. L. Li, Y. L. Xiao, S. T. Gan, Y. Zhang, Y. J. Li, X. R. Song, Q. Q. Xiong, S. J. Shi, Z. J. Li, W. Tao, H. Zhang, L. Mei and J. J. Shi, *Adv. Mater.*, 2018, 1803031.

45 G. Liu, H. I. Tsai, X. W. Zeng, J. Y. Qi, M. M. Luo, X. S. Wang, L. Mei and W. B. Deng, *Chem. Eng. J.*, 2019, **375**, 121917.

46 X. W. Zeng, W. Tao, L. Mei, Q. Huang, C. Y. Tan and S. S. Feng, *Biomaterials*, 2013, **34**, 6058–6067.

47 W. Tao, X. W. Zeng, J. Wu, X. Zhu, X. H. Yu, X. D. Zhang, J. X. Zhang, G. Liu and L. Mei, *Theranostics*, 2016, **6**, 470–484.

48 R. A. Gatenby, E. T. Gawlinski, A. F. Gmitro, B. Kaylor and R. J. Gillies, *Cancer Res.*, 2006, **66**, 5216–5223.

49 L. Bai, W. H. Yi, T. Y. Sun, Y. L. Tian, P. Zhang, J. H. Si, X. Hou and J. Hou, *J. Mater. Chem. B*, 2020, **8**, 6402–6417.

50 X. X. Han, J. Huang, H. Lin, Z. G. Wang, P. Li and Y. Chen, *Adv. Healthcare Mater.*, 2018, **7**, 1701394.

51 Z. Liu, H. Lin, M. L. Zhao, C. Dai, S. J. Zhang, W. J. Peng and Y. Chen, *Theranostics*, 2018, **8**, 1648–1664.

52 C. Dai, H. Lin, G. Xu, Z. Liu, R. Wu and Y. Chen, *Chem. Mater.*, 2017, **29**, 8637–8652.

53 T. Liu, Chao Wang, X. Gu, H. Gong, L. Cheng, X. Z. Shi, L. Z. Feng, B. Q. Sun and Z. Liu, *Adv. Mater.*, 2014, **26**, 3433–3440.

54 H. Lin, Y. W. Wang, S. S. Gao, Y. Chen and J. L. Shi, *Adv. Mater.*, 2018, **30**, 1703284.

55 B. G. Zhou, Y. Y. Pu, H. Lin, W. W. Yue, H. H. Yin, Y. F. Yin, W. W. Ren, C. K. Zhao, Y. Chen and H. X. Xu, *J. Mater. Chem. B*, 2020, **8**, 5257–5266.

56 R. L. Zhao, Q. L. Chen and Y. M. He, *Sci. Rep.*, 2018, **8**, 12680–12693.

This journal is © The Royal Society of Chemistry 2022

J. Mater. Chem. B, 2022, **10**, 1226–1235 | **1235**